Gradient scheme optimization for PRESS-localized edited MRS using weighted pathway suppression

Gizeaddis L. Simegn[1], Zahra Shams[1], Saipavitra Murali-Manohar[1], Dunja Simicic[1], Abdelrahman Gad[1], Yulu Song[1], Vivek Yedavalli[1], Christopher W. Davies-Jenkins[1], Aaron T. Gudmundson[1, 2], Helge J. Zöllner[1], Georg Oeltzschner[1], and Richard A.E. Edden[1,3,*]

1. The Russell H. Morgan Department of Radiology and Radiological Science, Johns Hopkins University School of Medicine, Baltimore, MD, USA.
2. The Malone Center for Engineering in Healthcare, Johns Hopkins University, Baltimore, MD, USA.
3. F.M. Kirby Research Center for Functional Brain Imaging, Kennedy Krieger Institute, Baltimore, MD, USA

*Corresponding Author:
Richard A. E. Edden, PhD
Russell H. Morgan Department of Radiology and Radiological Science
600 N. Wolfe St, Park 338,
Johns Hopkins University School of Medicine, Baltimore, MD, USA – 21287-0005

Abstract

This study aimed to design and implement an optimized gradient scheme for PRESS-localized edited magnetic resonance spectroscopy (MRS) to enhance suppression of out-of-voxel (OOV) artifacts. These artifacts, which originate from insufficient crushing of unwanted coherence transfer pathways (CTPs), are particularly challenging in editing schemes for metabolites like gamma-aminobutyric acid (GABA) and glutathione (GSH). To address this, a volume-based likelihood model was developed to guide gradient scheme optimization, prioritizing suppression of CTPs based on likelihood.

A volume-based likelihood model for CTP weighting was integrated into a Dephasing optimization through coherence order pathway selection (DOTCOPS) gradient optimization. Using a genetic algorithm with a new dual-penalty cost function, gradient schemes were optimized to maximize pathway-specific suppression. Hardware and sequence constraints, maximum gradient amplitudes and delay durations respectively, informed the optimization. Validation of the optimized scheme was performed with simulations and *in vivo* using an edited sequence in three brain regions (posterior cingulate cortex PCC, thalamus, and medial prefrontal cortex mPFC), with particular focus on OOV artifact reduction and spectral quality improvements.

The optimized gradient scheme demonstrated improved k-space crushing efficiency (by an average of 197%). OOV artifacts were reduced in all brain regions, particularly in highly OOV-susceptible regions (thalamus and mPFC). Improvements were most notable around 4.3 ppm with significant OOV amplitude reductions ($p < 0.001$).

By using a volume-based likelihood model for CTP prioritization, the optimized scheme ensures robust and region-agnostic performance in reducing OOV artifacts.

1. Introduction

Proton magnetic resonance spectroscopy (^{1}H MRS) is a non-invasive imaging modality that measures the *in vivo* concentration of metabolites in brain and body tissues, such as N-acetyl aspartate (NAA), choline-containing compounds (Cho), glutamate, glutamine, lactate, and others, which are potential biomarkers for conditions ranging from brain tumors to psychiatric disorders (1–6). MRS experiments are implemented as pulse sequences of radiofrequency (RF) and magnetic field gradient pulses, designed to control the evolution of the intended signals from the localized region of interest and suppress other potential nuisance signals. One useful tool for keeping track of the evolution of a given coherence through the pulse sequence is a coherence transfer pathway (CTP) diagram, which plots the coherence order at each stage of the sequence (7). Unwanted signals generally arise from different CTPs from the intended signals and degrade spectral quality and quantification accuracy (8,9). Among the most notorious of those nuisance signals are out-of-voxel (OOV) signals, spurious echoes from water signals outside the voxel refocused by local field gradients (10).

Low-concentration metabolites like γ-aminobutyric acid (GABA) are often measured with J-difference-edited MRS experiments (11) such a MEGA-PRESS (12) and Hadamard Editing Resolves Chemicals Using Linear-combination Estimation of Spectra (HERCULES) (13). CTP selection is particularly critical in edited MRS both because measurements of weak signals are less tolerant of small artifacts, and because edited MRS experiments have more RF pulses and sub-experiments than their unedited counterparts, increasing the number of CTPs to be controlled exponentially. Even considering only coherence orders ±1 and 0, a five-pulse sequence such as MEGA-PRESS yields 81 potentially detectable CTPs, of which only one corresponds to the desired metabolite signal.

Pulsed field gradients ("crusher gradients") are the primary mechanism for suppressing unwanted CTPs (14–16). These pulses, applied during evolution delays between RF pulses, impart phase shifts to coherences that depend on location and coherence order. An effective crusher gradient scheme results in the intended CTP being refocused, while unwanted CTPs accumulate destructive phase dispersion across the volume, effectively eliminating their signal contribution (17). Conventional gradient scheme designs often rely on heuristic strategies—iterative adjustments of gradient timing, duration, and amplitude until artifact-free spectra are empirically achieved. While this trial-and-error approach is feasible for basic localization sequences (e.g., PRESS or STEAM (18)), it becomes inadequate for advanced edited sequences due to the sheer number of pulses and gradients involved.

More systematic strategies, such as the Dephasing Optimization Through Coherence Order Pathway Selection (DOTCOPS) scheme (19,20), have formalized the design of crusher gradient schemes by using an algorithmic approach. DOTCOPS represented a significant advance over the traditional approach for MRS gradient scheme design for dephasing unwanted CTPs. The DOTCOPS optimization function considers all unwanted CTPs, using the 'k-space dephasing distance' as a proxy for pathway suppression, and seeking to maximize suppression of all pathways on average, and the least-suppressed pathway specifically. Although the option of differential weighting of pathways was suggested, in the absence of a theoretical basis to be more concerned with one CTP than another, no weightings were applied. In reality, not all unwanted CTPs pose the same risk to spectral quality, because some CTPs are more likely to be excited than others for a given pulse sequence configuration, and a model from which to calculate such weightings is required.

In this work, we introduce a volume-based model for CTP likelihood, and incorporate it into a weighted DOTCOPS gradient scheme optimization for PRESS-localized edited MRS. The proposed method introduces a pathway-specific suppression strategy, where CTPs are prioritized based on their likelihood of contributing to spectral contamination. This theory-guided weighting allows for a more intelligent allocation of gradient amplitudes, focusing suppression efforts on pathways that pose a greater risk to spectral quality and away from pathways that are improbable. The optimization is further guided by a new cost function that balances pathway suppression, emphasizing prioritized CTPs in both the minimum and average regularized suppression terms across all CTPs for globally consistent performance.

2. Methods

2.1. Coherence Transfer Pathway (CTP) likelihood model

All possible CTPs were systematically computed based on the sequence design, which includes five RF pulses. For each pulse, coherence orders were tracked, leading to 81 detectable pathways, representing all potential signal trajectories through the sequence. Each pathway's likelihood of contributing to the final acquired signal was estimated, and these values were used as weights during the gradient optimization. Pathway likelihoods were determined using a theoretical weighting scheme based on the expected contribution of each CTP to unwanted spectral contamination.

The likelihoods of each CTP were estimated by classifying the transition induced by each RF pulse based on the change in coherence order (Δp). Transitions with $\Delta p = \pm 2$ correspond to the action of 180° refocusing pulses, $\Delta p = \pm 1$ correspond to 90°-like pulses, and $\Delta p = 0$ lying outside the band of action, based on the principles of spin dynamics (21,22). These pulse

behaviors were then mapped onto specific spatial and spectral regions for slice- and frequency-selective pulses, respectively.

For the slice-selective excitation pulse, regions were treated as either “within-slice” or “out-of-slice”, corresponding to experienced flip angle of 90° or 0°, which we associate with CTPs of $\Delta p = \pm 1$ and $\Delta p = 0$, respectively. For slice-selective refocusing pulses, regions are classified as “within-slice,” “slice-edge,” or “out-of-slice”, corresponding to CTPs of $\Delta p = \pm 2, \pm 1$, and 0, respectively. For editing pulses, analogous categories were defined, “within-edit,” “edit-transition,” and “edit-off,” representing on-resonance, band-edge, and off-resonance effects. Relative probabilities were then assigned to reflect the extent of each region, reflecting its probability of contributing signal (see Figure 1). The values were based on the physical selectivity profiles of the RF pulses and the typical scenario of a voxel that is substantially smaller than the brain. Specifically, “within-slice” and “within-edit” transitions were assigned a baseline relative probability of 1. For slice-edge transitions, a lower probability of 0.2 was assigned reflecting the smaller extent of the transition band relative to the passband. In contrast, the large out-of-slice regions, which do not experience the RF pulse but may still undergo coherence evolution and refocusing (23), were heavily weighted with a probability of 10. For editing pulses, both within-edit and edit-transition spins were assigned equal probabilities of 1 due to the smoother transition profile of editing pulses which produce less rectangular inversion bands. Edit-off regions, being outside the editing band, were assigned a probability of 5, reflecting the greater extent of the chemical shift range relative to the editing pass band. We have chosen to represent these probabilities with integer estimates so they can be generally applied, rather than making accurate calculations of for one particular slice profile and voxel/head size.

The relative likelihood L(i) of a CTP i, consisting of the transitions $T_{i,n}$ (i.e., $\Delta p = 0, \pm 1, \pm 2$ occurring at pulse n in pathway i) in an N-pulse sequence then becomes the product of these transition probabilities as shown in Equation 1:

$$\mathrm{L}(i) = \prod_{n=1}^{N} P(T_{i,n}) \ , \qquad [1]$$

in which, $P(T_{i,n})$ is the probability weight assigned to that transition, based on spatial or spectral behavior ("within-slice", "edge", or "out-of-slice"), as summarized in Figure 1.

For the case of a 5-pulse sequence with 81 possible CTPs, corresponding to 405 total pathway transitions, almost half of all transitions are $\Delta p = \pm 1$, which is the lowest-likelihood action of every pulse. If all pathways are treated equally in gradient scheme optimization (as in previous work (19,20)), the large number of these low-likelihood CTPs can misdirect the focus of the optimizer. While DOTCOPS was always conceived with the option of weighting

CTPs differently, this 'volume-based likelihood' model provides a conceptual basis for the weights, allowing the optimization to prioritize the suppression of pathways that are more likely to generate out-of-voxel artifacts.

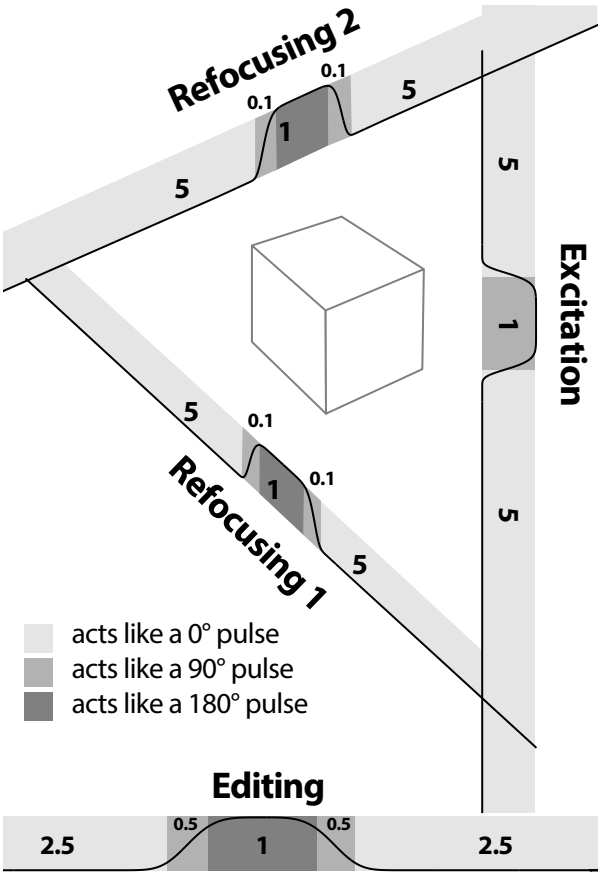

Figure 1: Estimation of CTP likelihoods based on the spatial and spectral profiles of RF pulse-induced transitions. For slice-selective pulses, transitions occurring within the excited region ("within-slice") are modeled as refocusing-like (Δp = ±2) and assigned a relative probability of 1. Regions within the excitation pulse passband and transitions at the edge of refocusing and editing pulses experience 90°-like pulses (associated with CTPS of Δp = ±1). The total transition-band probability is 0.2 for the refocusing pulse and 1 for the editing pulse. Out-of-band 'transitions' of Δp = 0 are given a higher likelihood of 10 for slice-selective pulses and 5 for editing pulses, reflecting the relative extent of each region. Note that transition-band and out-of-band regions occur on either side of the passband of each pulse, so the probabilities on each side are half the total likelihood values, respectively. Pulse profiles are for illustration purposes and are not accurate simulations.

2.2. Gradient scheme optimization

A gradient scheme was designed to increase suppression of unwanted CTPs in MEGA-edited PRESS-localized experiments (including HERCULES (13)), combining theory-driven weights, hardware- and sequence-informed constraints, and global optimization. The optimization aimed to adjust the gradient amplitudes across three axes (*x, y, z*) within the five sequence

delays. Gradient durations were constrained by the maximum available sequence delay between each pair of RF pulses: between the excitation pulse and first refocusing pulse; first refocusing pulse and first editing pulse; first editing pulse and second refocusing pulse; and between the second refocusing pulse and second editing pulse.

A genetic algorithm (GA) (*ga* function in MATLAB's Global Optimization Toolbox) was used for the optimization process due to its robustness in exploring high-dimensional and non-linear search spaces. The weighting w_i assigned to the ith pathway were calculated from L_i according to:

$$w_i = 0.1 + 0.9 * \left(\frac{L_i}{5}\right). \qquad [2]$$

The optimization objective was designed to balance two goals: ensuring sufficient gradient dephasing for the least-suppressed pathways and maintaining overall suppression efficiency as shown in Equation 3:

$$f(G) = -\left(min_{i=1\ to\ 80}\left(\frac{D_i}{w_i}\right) + \frac{1}{80}\sum_{i=1}^{80} D_i\ .\ w_i\right), \qquad [3]$$

where, w_i is the ith pathway normalized weighting (equal to L_i from Equation 1 and D_i is the L2 norm of net crusher moment for the ith pathway expressed as:

$$D_i = \sqrt{\sum_{k=1}^{3} M_{k,i}^2}\ , \qquad [4]$$

where $M = G \times P \in \mathbb{R}^{3X80}$ is the effective crusher moment for each pathway in each direction *k*, calculated as the matrix product of $G \in \mathbb{R}^{3X5}$, the gradient scheme, and $P \in \mathbb{R}^{5X80}$: the matrix of CTPs). To preserve the intended CTP, equality constraints were applied to balance the gradient moments. Specifically, the sum of the second and third gradient areas in each direction was constrained to equal the combined areas of the first, fourth and fifth gradient areas, in line with refocusing the desired pathway of p = (-1, +1, +1, -1, -1).

While most gradient durations were constrained to fill their respective delays, a 1 ms delay was reserved after the final gradients to mitigate the effects of eddy currents and hardware-induced phase distortions on the acquired signal.

2.3. Gradient-scheme-induced diffusion weighting

The incidental diffusion weighting due to the elongated duration of the new crusher schemes is estimated by calculating the b-value and signal loss according to reference (24), as in Equation 5:

$$b = \gamma^2 \int_0^{TE} \left(\int_0^t G(t')\, dt' \right)^2 dt, \qquad [5]$$

where γ is the gyromagnetic ratio (267.522×10^6 rad/T/s), $G(t)$ is time-dependent gradient waveform (in *T/m*) and TE is the echo time (in *s*). The total b-value, which includes the diffusion due to the interaction of gradient pairs, can be calculated from the self-term (contribution of diffusion weighting from a single isolated gradient pulse) and cross-term contributions (due to the overlapping gradients i and j on different axes (e.g., *x* and *y*) in different axes):

$$b_{total} = \sum_{axes} \left(\sum_{i=1}^{N} b_{self,i} + \sum_{i=1}^{N} \sum_{j=1}^{N} b_{cross,i,j} \right). \qquad [6]$$

Then, the signal attenuation due to diffusion can be calculated from b_{total} given the average diffusion coefficient D_{av} of metabolites or tissue water:

$$\frac{S}{S_0} = e^{(-b_{total} D_{av})} \qquad [7]$$

2.4. MRS data acquisition

The performance of the optimized gradient scheme was assessed by *in vivo* MRS experiments on ten healthy volunteers (4 females, 6 males, age 26.3±3.4 years). All volunteers provided written informed consent to participate. The Johns Hopkins University Institutional Review Boards approved all study procedures. All scans were conducted on a 3T Philips dStream Ingenia Elition MRI scanner (Philips Healthcare, Best, The Netherlands) using a 32-channel head coil. For MRS voxel placement, a T_1-weighted structural MPRAGE scan was acquired with the following parameters: TR/TE = 8.0 ms/3.7 ms; flip angle 8°; slice thickness 1.0 mm; 150 slices; isotropic voxel size of 1 mm^3, accelerated by compressed sensing with a total acquisition time of 2 minutes and 46 seconds. Following structural imaging, data were acquired using the HERCULES (13) protocol from 30 x 30 x 30 mm^3 voxels centered on posterior cingulate cortex (PCC), followed by 23 x 30 x 23 mm^3 voxels centered on thalamus, and 23 x 23 x 23 mm^3 voxels centered on medial prefrontal cortex (mPFC) (AP × RL × FH) (as shown in Figure 2). Scan parameters for HERCULES were: TR/TE = 2000 ms /80 ms; 192 transients sampled at 2000 Hz with 2048 points; and VAPOR

(25) water suppression. For each subject, data were acquired twice — once using the "two-last, increased-area" (recently demonstrated to suppress OOV signal more than our prior gradient scheme (26)) and once using the newly optimized ("delay-filling optimized") gradient schemes, compared on Figure 3. Identical voxel positioning and sequence parameters were maintained for both acquisitions to ensure a fair comparison.

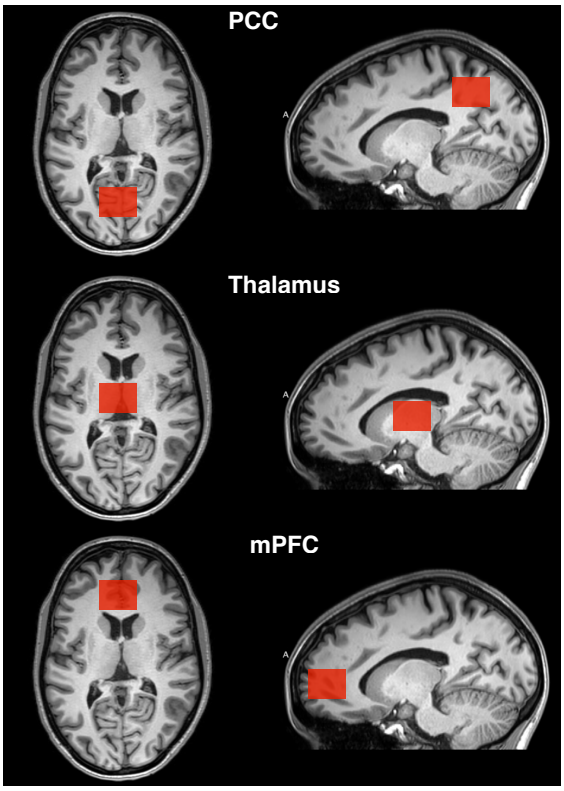

Figure 2: MRS Voxel placement. In vivo edited spectra were acquired from a (30 × 30 × 30) mm^3 posterior cingulate cortex (PCC), a (23 × 30 × 23) mm^3 thalamus and a (23 × 23 × 23) mm^3 medial prefrontal (mPFC) voxels.

2.5. MRS data processing and analysis

The edited MRS data were analyzed within MATLAB R2023b using the open-source MRS analysis toolbox Osprey v2.9 (27), following consensus-recommended preprocessing and linear-combination modeling. Frequency and phase correction of FIDs was achieved via robust spectral registration (28). A Hankel singular value decomposition (HSVD) filter was applied to suppress residual water. Linear-combination modeling (LCM) was performed on each of the relevant Hadamard spectrum combinations (i.e., SUM; the sum of all sub-spectra acquired across all sub-experiments, GABA-edited, and GSH-edited difference spectra) from 0.2 to 4.5 ppm, using 17 metabolite basis functions (including Ascorbate (Asc), Aspartate (Asp), Creatine (Cr), Gamma-Aminobutyric Acid (GABA), Glycerophosphocholine (GPC), Glutathione (GSH), Glutamine (Gln),

Glutamate (Glu), Myo-Inositol (Ins), Lactate (Lac), N-Acetylaspartate (NAA), N-Acetylaspartylglutamate (NAAG), Phosphocholine (PCh), Phosphocreatine (PCr), Phosphoethanolamine (PE), and Scyllo-Inositol (sI), Taurine (Tau)) and 8 macromolecule (MM) and lipid components parameterized as Gaussians for the sum spectrum. For GSH-edited spectra, MM peaks at 1.2 and 1.4 ppm were modeled, while GABA-edited spectra included a composite MM basis function with peaks at 3 and 0.93 ppm (29) with a 3 to 2 amplitude ratio. Soft amplitude constraints were applied for MM, lipids, and NAAG/NAA ratios, based on values described in the LCModel manual (30).

2.6. OOV artifact quantification

To compare the new and old gradient schemes in reducing artifacts, the relative amplitude of OOV signals for each Hadamard combination spectrum, calculated by Osprey as a quality metric (QM) and quantified using Equation 6, was used.

$$\text{Relative OOV} = \frac{\sum_{ppm=3.9}^{ppm=4.5} residual^2}{std(noise)^2 * n} \qquad [6]$$

where *residual* refers to the LCM residual between 3.9 to 4.5 ppm (the region of the spectrum with most prominent OOV signals), *std* is the standard deviation, *noise* refers to the real part of noise of the spectrum between −2 and 0 ppm, and *n* is the number of points in the model range.

2.7. Statistical Analysis

To evaluate whether residuals from OOV echoes differed between the new "delay-filling optimized" and the old "two-last, increased-areas" gradient schemes, a multi-way (three-way) analysis of variance (ANOVA) was used. The analysis examined the effects of three factors: 'Subject', 'Voxel location', and 'Gradient scheme' on the mean relative OOV values derived from the SUM, GABA-edited, and GSH-edited spectra. Differences in mean relative OOV values across factor levels were assessed using F-statistics and associated p-values (Prob > F), with statistical significance defined at the 0.05 level.

3. Results

3.1. Optimized gradient scheme and total crushing moment across CTPs

The "delay-filling optimized" and the "two-last, increased-area" gradient schemes are compared in Figure 3. The genetic algorithm maximized the gradient areas across all three

axes, except for the second gradient in each, while reversing the polarity of the first two gradients in the second axis (G_y).

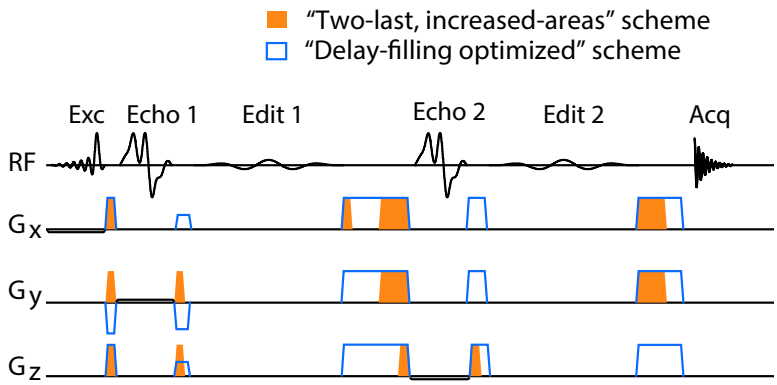

***Figure 3**: "Delay-filling optimized" (blue) and "Two-last, increased-area" (orange) gradient schemes*

The total crushing moment (k-space crushing distance) of each CTP for the "delay-filling optimized" and the "two-last, increased-area" (26), are compared in Figure 4. Each column in the plot represents one of the 81 potential pathways and is aligned with the relevant column of the CTP map, in which where each row indicates the coherence order after a given RF pulse (RF_{ex}, RF_{echo1}, RF_{edit1}, RF_{echo2}, RF_{edit2}). By convention, the final coherence order of –1 corresponds to the detected signal. The total crushing distance in k-space for each pathway is compared for the two gradient schemes (blue and orange). The optimization weighting assigned to each pathway is represented by the background of the plot. As shown, the new optimized gradient scheme achieves a larger crushing moment for most unwanted CTPs than the other approach, and especially for likely CTPs, demonstrating its potential for more effectively minimizing OOV artifacts.

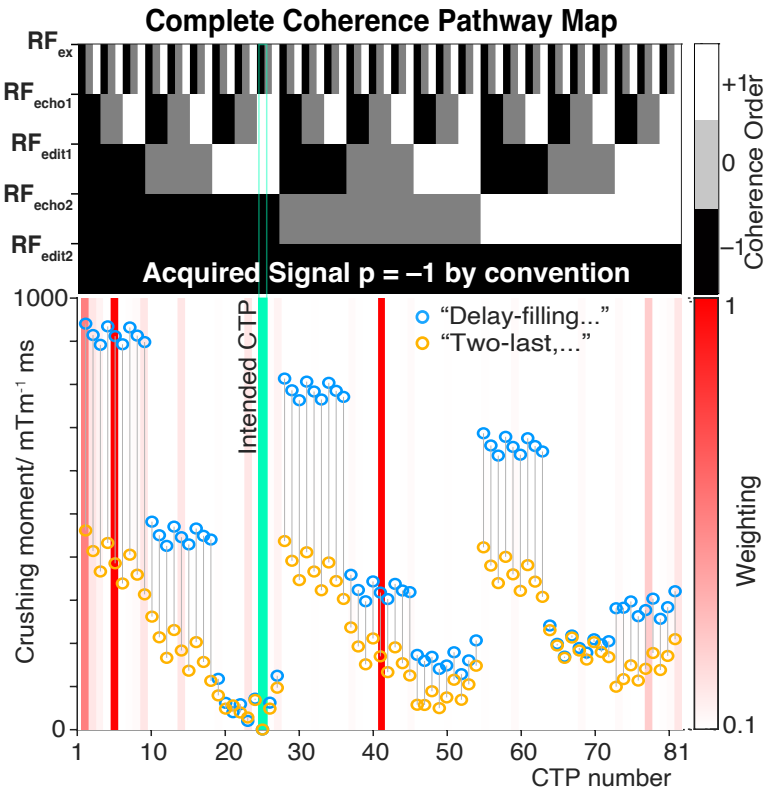

***Figure 4**: Comparison of total crushing moments of each coherence transfer pathways (CTP) for the "delay-filling optimized" and "two-last, increased-area" gradient schemes. The full CTP map, where each column represents one of the 81 possible pathways and each row shows the coherence order after an RF pulse. Coherence orders are color-coded: +1 in white, 0 in gray, and –1 in black. Total crusher moments (in mT·m $^{-1}$·ms) are plotted for each scheme, "delay-filling optimized" in blue and "two-last, increased areas" in orange. The background shows the weightings of each CTP. The "delay-filling optimized" scheme clearly increases crushing moments for most unwanted CTPs, suggesting it may more effectively suppress unwanted signal pathways.*

3.2. Comparison of *in vivo* data

Representative spectral comparisons between the "delay-filling optimized" and the "two-last, increased-area" scheme across three brain regions: PCC, thalamus, and mPFC, are shown in Figure 5. For each region, the SUM, GABA-edited, and GSH-edited difference spectra are shown alongside their respective model fits and residuals. In the thalamus (Figure 5A) and mPFC (Figure 5B), the "delay-filling optimized" scheme clearly demonstrates reduced OOV artifacts, as indicated by lower residual signals, particularly around 4.3 ppm. This improvement shows the effectiveness of the delay-filling optimization in minimizing OOV contamination, particularly in regions prone to susceptibility-related artifacts.

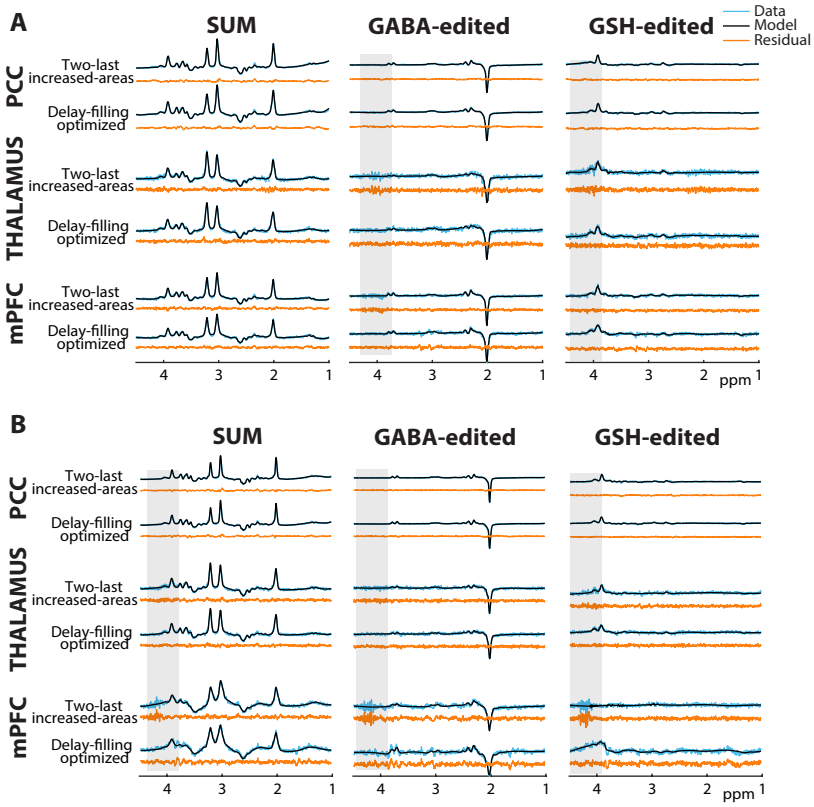

Figure 5*: Spectra and model-residual comparisons between the "delay-filling optimized" gradient scheme and the "two-last, increased-area" gradient scheme, using data from two representative volunteers across three brain regions: PCC, thalamus, and mPFC. Each panel shows the SUM spectrum, GABA-edited, and GSH-edited difference spectra (blue), their respective model fits (black), and residuals (orange). The delay-filling optimized gradient scheme shows reduced OOV artifacts in the thalamus (Figure 4A) and mPFC (Figure 4B) compared to the alternative scheme (highlighted in gray).*

3.3. OOV artifact quantification

The relative amplitude of OOV residuals across subjects and brain regions is compared using box plots in Figure 6 and using a three-way ANOVA in Table 1. There is a strong main effect of gradient scheme ($p < 0.001$), indicating that the delay-filling optimized scheme significantly reduced artifacts compared to the other scheme. There was also a significant effect of subject ($p < 0.001$), showing expected variability in data quality based on individual anatomy. In contrast, voxel location did not have a significant overall impact ($p = 0.248$). A significant interaction was found between subject and voxel location ($p < 0.001$), and a three-way interaction among subject, location, and gradient scheme was also significant ($p = 0.048$), pointing to some variability in how the new scheme performed depending on both the individual and the voxel location. Overall, these results support the effectiveness of the optimized gradient scheme in reducing OOV-related artifacts.

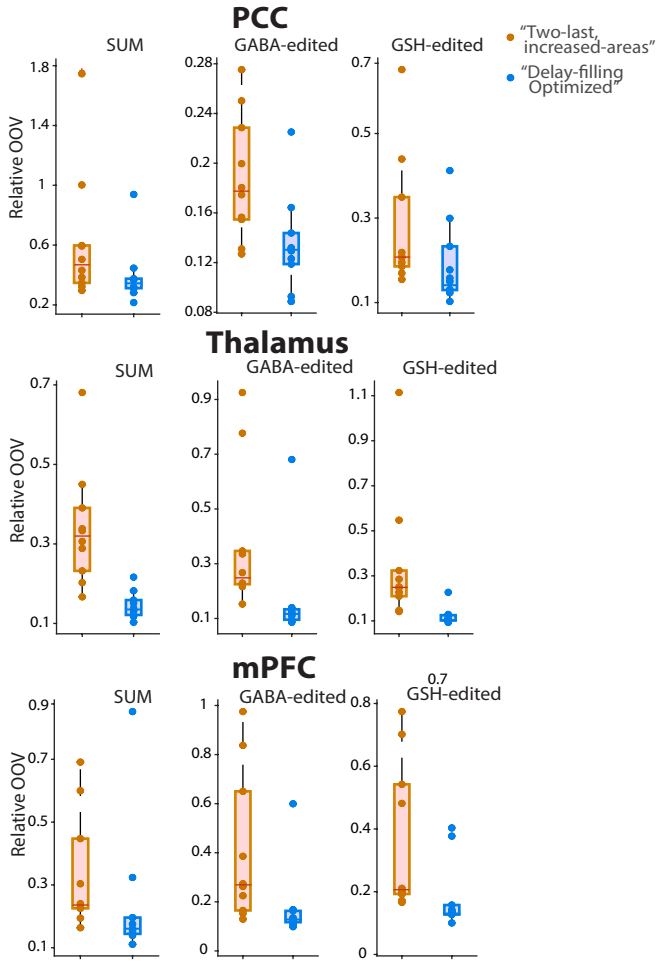

***Figure 6**: Comparison of relative OOV values (model residuals) across 10 datasets using the* "two-last, increased-areas" *scheme (orange) and the* "delay-filling optimized" *scheme (blue). Each data point (filled circle) represents the relative OOV values from an individual dataset.*

***Table 1**: Summary of three-way ANOVA results evaluating the effects of subject, voxel location, and gradient scheme (delay-filling optimized vs. two-last, increased-areas) on the relative OOV. A significant main effect of gradient scheme indicates that the optimized scheme substantially reduced OOV artifacts. Significant interactions suggest variability in the effect across subjects and regions (Sum Sq.* – Sum of Squares, *Mean Sq.* – Mean Square, *F* – F-statistic, *p-value* – Probability Value*).*

Analysis of Variance (ANOVA)					
Source	Sum Sq.	d.f.	Mean Sq.	F	*p*-value
Subject	1.43	9	0.16	5.50	< 0.001
Voxel location	0.08	2	0.04	1.41	0.24
Gradient scheme	1.23	1	1.23	42.38	< 0.001
Subject x Voxel location	2.04	18	0.11	3.91	< 0.001
Subject x Gradient scheme	0.51	9	0.07	1.94	0.05
Voxel location x Gradient scheme	0.05	2	0.03	0.93	0.39
Subject x Voxel location x Gradient scheme	0.89	18	0.05	1.70	0.04

3.4. Gradient scheme-induced diffusion weighting

The incidental diffusion weighting introduced by the delay-filling optimized gradient scheme resulted in a total b-value of approximately 831.21 s/mm^2. Based on this b-value and the known apparent diffusion coefficients (ADC), 1.6 × 10^{-4} mm^2/s for tNAA, 1.41 × 10^{-4} mm^2/s for tCho, 1.5 × 10^{-4} mm^2/s for Glu, 1.44 × 10^{-4} mm^2/s for tCr, and 7.8 × 10^{-4} mm^2/s for water (31), we estimated the corresponding signal attenuation (S/S_0) for each. The results showed modest signal reductions for metabolites in the range of 11–12%. Water exhibited a higher attenuation, with an S/S_0 of 0.6. The estimated values agree with the experimental data acquired as shown in Figure 7.

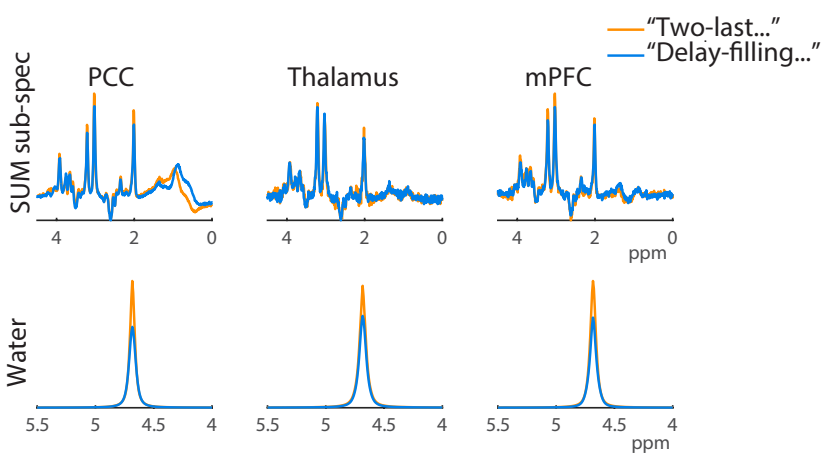

Figure 7:Comparisons of signal amplitudes acquired using the "two-last, increased-areas" and "delay-filling optimized" gradient schemes, illustrating diffusion losses.

4. **Discussion**

OOV artifacts are a long-standing challenge for single-voxel spectroscopy, obstructing metabolite signals and interfering with data processing algorithms. These unwanted signals are particularly pronounced in edited MRS due to the larger number of CTPs possible and the low amplitude of target signals, such as GABA and GSH. OOV signals originate from outside of the shimmed voxel of interest from pathways refocused by local field inhomogeneities. As each artifact arises from a specific coherence transfer pathway, it is critical to develop a tailored gradient scheme capable of suppressing coherence transfer pathways that are most likely to arise.

In this work, we presented a volume-based likelihood model for coherence transfer pathway weighting, integrated within a DOTCOPS-based gradient optimization framework for PRESS-localized edited MRS. Our approach aimed to prioritize suppression based on the estimated spectral contamination likelihood of each CTP, thereby enabling a more targeted and efficient use of gradient areas. The cost function used for gradient scheme optimization has two terms: one that prioritizes suppression of the least-crushed CTP and one that prioritizes suppression on average. It is notable that the weightings are applied in this optimization in a different fashion than anticipated (but not used) in the DOTCOPS optimizer. In this implementation, important terms are emphasized in the mean by multiplied weights, and we make it more likely that a prioritized CTP would be considered by the minimum term by division of weights. In MEGA-edited PRESS sequences, the delays can have very different durations, and until now we have largely ignored this opportunity for increased CTP selectivity. The proposed model reflects a shift from the "one-size-fits-all" gradient approach (adapting MEGA-PRESS scheme only slightly from its parent PRESS) to a strategy that is more adaptive and efficient for OOV artifact reduction.

Using the proposed delay-filling and volume-based CTP likelihood weighting strategy, the genetic algorithm produced a scheme that maximized gradient areas across all three spatial axes with mixed polarity in the second axis. In terms of optimizer cost function, there are six variations on this scheme that have degenerate costs – each gradient axis independently can be inverted without changing the overall cost, as noted in the original DOTCOPS paper (19). While degenerate in terms of cost, these schemes are different in terms of the spatial origin of OOV signals that might arise (32). When evaluated in terms of total k-space crushing moment across CTPs, the “delay-filling optimized” scheme performed better than the “two-last, increased-area” approach, which was recently shown to perform better than our default.

These theoretical improvements were borne out in the *in vivo* data. Across three regions, the PCC, thalamus, and mPFC, the optimized gradient scheme showed reduced OOV artifacts, particularly around 4.3 ppm (as shown in Figure 5). Notably, the thalamus and mPFC, which are highly susceptible to B_0 inhomogeneities and edge effects due to their proximity to air-tissue interfaces, showed more OOV signal and thus more opportunity for improved suppression, validating the robustness of the optimized scheme. The fact that voxel location

did not exhibit a main effect (p = 0.248) suggests that the optimized scheme performs reliably across varied anatomical regions. Some inter-subject and voxel-scheme interaction effects were observed, which is not unexpected given known variability in head shape, positioning, and susceptibility distributions (33), The general trend favored the delay-filling optimized gradient scheme.

A key consideration in optimizing gradient schemes is the influence of diffusion effects, which can significantly impact metabolite quantification. Even within MRS sequences not primarily designed for diffusion measurements, some degree of diffusion sensitivity is inherently present due to gradients. Particularly for the maximalist scheme optimized here, which makes full use of gradient amplitude and duration limits, it is essential to quantify diffusion weighting through b-value calculations. In our study, the optimized crusher scheme introduced an effective b-value of approximately 831 s/mm^2**,** which resulted in an estimated 8–12% signal attenuation for metabolites. This level of diffusion weighting would require additional correction terms for absolute quantification. The observed diffusion attenuation was much stronger (~40%) on the unsuppressed water reference signal, due to the more rapid diffusion of water. For quantitative MRS, it is common to acquire one water reference signal for eddy current correction (34) at long-TE, as here, and an additional reference at short-TE with less relaxation weighting. This second reference would be especially important with this degree of diffusion weighting. The Integrated Short-TE and Hadamard-edited Multi-Sequence (ISTHMUS) (35) automatically acquires long- and short TE water references, but for other sequences reference experiments are separately acquired.

Although this study focused on PRESS-localized edited MRS, the optimized scheme could be extended to other sequences, such as STEAM or semi-LASER, which involve different coherence pathway dynamics and gradient requirements. In this work, we treated the underlying sequence timing as fixed and optimized the gradient areas within the available delays. MEGA-PRESS does have two degrees of freedom – the duration of the first and second slice-selective echo pulses, and the relative timing of slice-selective and editing pulses. These internal sequence delays could be varied within the optimizer in future work. Additionally, the interaction between diffusion-induced signal attenuation and improved suppression could be modeled more explicitly in future optimization frameworks. Incorporating diffusion weighting into the algorithm, for instance by penalizing excessive signal attenuation during b-value estimation, could maintain effective OOV suppression with lower levels of diffusion weighting.

5. Conclusion

In this study, we proposed and implemented an optimized gradient scheme for PRESS-localized edited MRS, using a volume-based likelihood model prioritizing CTPs based on spectral contamination likelihood. Using a genetic algorithm optimization and a delay-filling based approach, the resulting scheme demonstrated significant improvements in k-space

crushing and suppression of unwanted pathways. *In vivo* validation across brain regions, including the PCC, thalamus, and mPFC, showed a reduction in OOV artifacts and improved spectral quality, even in regions prone to susceptibility challenges.

Acknowledgements

This work was supported by NIH grants R01 EB016089, R01 EB023963, R01 EB032788, R01 EB035529, R21 EB033516, R00 AG02230, K99 AG080084, and P41 EB031771. GO is a paid consultant for Neurona Therapeutics Inc (unrelated to this work).

Author Contributions

GLS contributed to Conceptualization, Methodology, Software, Validation, Formal Analysis, Investigation and Writing. ZS contributed to the Data Acquisition, Investigation, Resources and Data Analysis. SMM contributed to Data Acquisition, Writing, and Visualization. DS contributed to Data Acquisition, Writing, and Visualization. AG contributed to Data acquisition, Writing, and Visualization. YS contributed to Writing, and Visualization. VY contributed to the Investigation and Resources. CWD contributed to Writing, and Visualization. ATG contributed to Writing, and Visualization. HJZ contributed to Software, Formal Analysis, Writing, and Visualization. GO contributed to Software, Formal Analysis, and Supervision. RAEE contributed to Conceptualization, Methodology, Software, Validation, Formal Analysis, Investigation, Visualization, Writing, Supervision, Project Administration, and Funding Acquisition.

References

1. Tran T, Ross B, Lin A. Magnetic Resonance Spectroscopy in Neurological Diagnosis. Neurol Clin. 2009 Feb 1;27(1):21–60.

2. Lee MR, Denic A, Hinton DJ, Mishra PK, Doo-Sup, Pirko I, et al. Preclinical 1H-Mrs Neurochemical Profiling in Neurological And Psychiatric Disorders. Bioanalysis. 2012 Jul 1;4(14):1787–804.

3. Maddock RJ, Buonocore MH. MR spectroscopic studies of the brain in psychiatric disorders. Curr Top Behav Neurosci. 2012;11:199–251.

4. Ford TC, Crewther DP. A Comprehensive Review of the 1H-MRS Metabolite Spectrum in Autism Spectrum Disorder. Front Mol Neurosci. 2016 Mar 9;9:9:14.

5. Koush Y, Rothman DL, Behar KL, de Graaf RA, Hyder F. Human brain functional MRS reveals interplay of metabolites implicated in neurotransmission and neuroenergetics. J Cereb Blood Flow Metab. 2022 Jun;42(6):911–34.

6. Ryberg M, Boraxbekk CJ, Kjaer M, Demnitz N. Effects of acute physical activity on brain metabolites as measured by magnetic resonance spectroscopy (1H-MRS) in humans: A systematic review. Heliyon. 2023 Oct 1;9(10).

7. Bain AD. Coherence levels and coherence pathways in NMR. A simple way to design phase cycling procedures. J Magn Reson 1969. 1984 Feb 15;56(3):418–27.

8. Kreis R. Issues of spectral quality in clinical 1H-magnetic resonance spectroscopy and a gallery of artifacts. NMR Biomed. 2004 Oct;17(6):361–81.

9. Song Y, Zöllner HJ, Hui SCN, Hupfeld KE, Oeltzschner G, Edden RAE. Impact of gradient scheme and non-linear shimming on out-of-voxel echo artifacts in edited MRS. NMR Biomed. 2023;36(2):e4839.

10. Starck G, Carlsson A, Ljungberg M, Forssell-Aronsson E. k-space analysis of point-resolved spectroscopy (PRESS) with regard to spurious echoes in in vivo (1)H MRS. NMR Biomed. 2009 Feb;22(2):137–47.

11. Rothman DL, Petroff OA, Behar KL, Mattson RH. Localized 1H NMR measurements of gamma-aminobutyric acid in human brain in vivo. Proc Natl Acad Sci U S A. 1993 Jun 15;90(12):5662–6.

12. Mescher M, Merkle H, Kirsch J, Garwood M, Gruetter R. Simultaneous in vivo spectral editing and water suppression. NMR Biomed. 1998;11(6):266–72.

13. Oeltzschner G, Saleh MG, Rimbault D, Mikkelsen M, Chan KL, Puts NAJ, et al. Advanced Hadamard-encoded editing of seven low-concentration brain metabolites: Principles of HERCULES. NeuroImage. 2019 Jan 15;185:181–90.

14. Hurd RE. Gradient-enhanced spectroscopy. J Magn Reson 1969. 1990 Apr 1;87(2):422–8.

15. Jerschow A, Muller N. Efficient simulation of coherence transfer pathway selection by phase cycling and pulsed field gradients in NMR. J Magn Reson San Diego Calif 1997. 1998 Sep;134(1):17–29.

16. Rodriguez I, Alejo RP de, Ruiz-Cabello J. Pathway selection by pulsed field gradients. Magn Reson Med. 2002;48(3):540–2.

17. Ernst T, Chang L. Elimination of artifacts in short echo time H MR spectroscopy of the frontal lobe. Magn Reson Med. 1996 Sep;36(3):462–8.

18. Frahm J, Merboldt KD, Hänicke W. Localized proton spectroscopy using stimulated echoes. J Magn Reson 1969. 1987 May 1;72(3):502–8.

19. Landheer K, Juchem C. Dephasing optimization through coherence order pathway selection (DOTCOPS) for improved crusher schemes in MR spectroscopy. Magn Reson Med. 2019;81(4):2209–22.

20. Landheer K, Juchem C. Simultaneous optimization of crusher and phase cycling schemes for magnetic resonance spectroscopy: an extension of dephasing optimization through coherence order pathway selection. Magn Reson Med. 2020 Feb;83(2):391–402.

21. Levitt MH. Spin Dynamics: Basics of Nuclear Magnetic Resonance. John Wiley & Sons; 2008. 767 p.

22. Ernst RR. Title Pages. In: Ernst RR, Bodenhausen G, Wokaun A, editors. Principles of Nuclear Magnetic Resonance in One and Two Dimensions. Oxford University Press; 1990. p. 0. (International Series of Monographs on Chemistry).

23. Edden RAE, Barker PB. Spatial effects in the detection of γ-aminobutyric acid: Improved sensitivity at high fields using inner volume saturation. Magn Reson Med. 2007;58(6):1276–82.

24. Mori S, van Zijl PC. Diffusion weighting by the trace of the diffusion tensor within a single scan. Magn Reson Med. 1995 Jan;33(1):41–52.

25. Tkác I, Starcuk Z, Choi IY, Gruetter R. In vivo 1H NMR spectroscopy of rat brain at 1 ms echo time. Magn Reson Med. 1999 Apr;41(4):649–56.

26. Shams Z, Gad A, Gudmundson AT, Murali-Manohar S, Davies-Jenkins CW, Simegn GL, et al. Identifying out-of-voxel echoes in edited MRS with phase cycle inversion [Internet]. bioRxiv; 2025 [cited 2025 Jul 7]. p. 2025.06.26.661810. Available from: https://www.biorxiv.org/content/10.1101/2025.06.26.661810v1

27. Oeltzschner G, Zöllner HJ, Hui SCN, Mikkelsen M, Saleh MG, Tapper S, et al. Osprey: Open-source processing, reconstruction & estimation of magnetic resonance spectroscopy data. J Neurosci Methods. 2020 Sep 1;343:108827.

28. Mikkelsen M, Tapper S, Near J, Mostofsky SH, Puts NAJ, Edden RAE. Correcting frequency and phase offsets in MRS data using robust spectral registration. NMR Biomed. 2020 Oct;33(10):e4368.

29. Zöllner HJ, Tapper S, Hui SCN, Barker PB, Edden RAE, Oeltzschner G. Comparison of linear combination modeling strategies for edited magnetic resonance spectroscopy at 3 T. NMR Biomed. 2022;35(1):e4618.

30. Provencher SW. “LCModel & LCMgui user’s manual.” LCModel version. 2014;6(3).

31. Deelchand DK, Auerbach EJ, Marjańska M. Apparent diffusion coefficients of the five major metabolites measured in the human brain in vivo at 3 T. Magn Reson Med. 2018 Jun;79(6):2896–901.

32. Shams Z, Klomp DWJ, Boer VO, Wijnen JP, Wiegers EC. Identifying the source of spurious signals caused by B0 inhomogeneities in single-voxel 1H MRS. Magn Reson Med. 2022;88(1):71–82.

33. Wilson M, Andronesi O, Barker PB, Bartha R, Bizzi A, Bolan PJ, et al. A Methodological Consensus on Clinical Proton MR Spectroscopy of the Brain: Review and Recommendations. Magn Reson Med. 2019 Aug;82(2):527–50.

34. Klose U. In vivo proton spectroscopy in presence of eddy currents. Magn Reson Med. 1990 Apr;14(1):26–30.

35. Hui SCN, Murali-Manohar S, Zöllner HJ, Hupfeld KE, Davies-Jenkins CW, Gudmundson AT, et al. Integrated Short-TE and Hadamard-edited Multi-Sequence (ISTHMUS) for advanced MRS. J Neurosci Methods. 2024 Sep;409:110206.